EES Batteries

PAPER

View Article Online
View Journal | View Issue

Cite this: *EES Batteries*, 2026, **2**, 639

Unraveling interphase-driven failure pathways in $LiMn_{0.6}Fe_{0.4}PO_4$/graphite pouch cells

Chanmonirath (Michael) Chak, [a] Vadim Shipitsyn, [a] Ruyi Song, [b] Glenn Pastel, *[c] Wenhua Zuo, [d] Yuwei Zhu, [e] Gui-Liang Xu, [d] Linqin Mu [e] and Lin Ma *[a]

$LiMn_xFe_{1-x}PO_4$ (LMFP) is a promising high-voltage, thermally stable, and earth-abundant cathode material, yet its practical application is limited by interphase instability and Mn dissolution. In this work, we systematically evaluate $LiMn_{0.6}Fe_{0.4}PO_4$/graphite pouch cells using three electrolyte formulations including control carbonate electrolyte, control + 2 wt% vinylene carbonate (VC), and control + 2 wt% VC + 1 wt% 1,3,2-dioxathiolane 2,2-dioxide (DTD), to establish how electrolyte composition governs interphase chemistry and long-term degradation. Electrochemical testing shows that both additives are preferentially reduced prior to ethylene carbonate (EC) during cell formation, generating robust cathode-electrolyte interphase (CEI) and solid-electrolyte interphase (SEI) layers that suppress gas evolution and raise the first-cycle coulombic efficiency to 89.3%. Additionally, the dual-additive electrolyte delivers the most stable performance, retaining over 85% capacity after 600 cycles while minimizing impedance growth under long-term cycling at C/3 and 40 °C. Soft X-ray absorption spectroscopy confirms that VC + DTD effectively suppresses electrolyte oxidation at the cathode surface, and micro-X-ray fluorescence shows substantially reduced Mn dissolution and deposition on the graphite anode. Density functional theory simulations further provided insights into the structural and energetic influences of alkoxide species on the cathode surface, proposing a Mn^{2+} extraction mechanism. The combined experimental and computational findings establish a mechanistic link between electrolyte composition and interphase evolution, highlighting the effectiveness of electrolyte engineering for extending the operational lifetime of LMFP-based lithium-ion batteries.

Received 8th December 2025,
Accepted 13th January 2026

DOI: 10.1039/d5eb00228a

rsc.li/EESBatteries

Broader context

As demand grows for safe, durable, and resource-sustainable lithium-ion batteries, $LiMn_xFe_{1-x}PO_4$ (LMFP) has emerged as an attractive high-voltage, earth-abundant cathode material that avoids reliance on nickel and cobalt. Yet, its practical deployment is constrained by Mn dissolution and unstable electrode–electrolyte interphases (EEIs) that accelerate performance degradation. Although electrolyte additives such as vinylene carbonate (VC) and 1,3,2-dioxathiolane 2,2-dioxide (DTD) have shown promise in stabilizing these interphases and suppressing parasitic reactions, the mechanistic basis of these improvements in LMFP systems remains insufficiently resolved. By integrating long-term cycling with advanced X-ray spectroscopy and theoretical modeling analysis, this study uncovers how electrolyte composition governs interphase chemistry and Mn-dissolution pathways in LMFP/graphite cells, providing fundamental insight into degradation of their effectiveness and demonstrating how targeted electrolyte modification can strengthen interphase stability and enhance cycling resilience.

1. Introduction

Lithium-ion batteries (LIBs) power a broad range of applications, from portable electronics to emerging sectors such as electric vehicles, drones, and energy-intensive AI data centers, driving the global transition toward electrification.[1] Among LIB cathode chemistries, $LiFePO_4$ (LFP) has gained prominence for large-scale deployments, particularly in applications involving human proximity, owing to its exceptional safety, and long cycle lifetime. However, its relatively low operating

[a]*Department of Applied Physical Sciences, University of North Carolina at Chapel Hill, Chapel Hill, NC 27514, USA. E-mail: l.ma@unc.edu*
[b]*DP Technology, Delaware, USA*
[c]*Battery Sciences Branch, DEVCOM Army Research Laboratory, Adelphi, MD 20783, USA. E-mail: glenn.r.pastel.civ@army.mil*
[d]*Chemical Sciences and Engineering Division, Argonne National Laboratory, Lemont, IL 60439, USA*
[e]*Materials Science Engineering, School of Engineering for Matter, Transport, and Energy, Arizona State University, Tempe, AZ 85281, USA*

voltage (~3.5 V *vs.* Li/Li^+)[2] and modest theoretical specific capacity (170 mAh g^{-1}, practically 120–160 mAh g^{-1}) impose fundamental limitations on energy density.

$LiMn_xFe_{1-x}PO_4$ (LMFP), which retains the robust olivine structure of LFP, has emerged as a highly promising next-generation phosphate cathode. By partially substituting Fe with Mn, LMFP activates the Mn^{2+}/Mn^{3+} redox couple at ~4.1 V *vs.* Li/Li^+ in addition to the Fe^{2+}/Fe^{3+} couple at ~3.5 V *vs.* Li/Li^+, delivering 10–20% higher energy density while preserving comparable thermal stability and intrinsic safety.[2–4] Moreover, LMFP eliminates reliance on scarce and costly nickel and cobalt, instead leveraging earth-abundant, low-cost, and environmentally benign iron and manganese, making it particularly attractive for sustainable, gigawatt-scale manufacturing. Despite these advantages, widespread commercialization of LMFP remains hindered by several critical challenges. Chief among them is accelerated capacity fade caused by disproportionate Jahn–Teller distortion of Mn^{3+}, which induces lattice strain and micro-cracking during cycling.[5] Mn dissolution, driven by the disproportionate reaction $2Mn^{3+} \rightarrow Mn^{4+} + Mn^{2+}$ and subsequent Mn^{2+} leaching into the electrolyte, further exacerbates transition-metal loss, triggering parasitic side reactions and degradation of the anode solid-electrolyte interphase (SEI).

Electrolyte engineering represents one of the most effective strategies for enhancing the electrochemical stability and cycle life of LIBs by precisely tailoring the electrode–electrolyte interphase (EEI). Recent advances in electrolyte design have leveraged tailored salt formulations and solvation structures to enable moisture-tolerant, high-voltage (up to 4.6 V) and wide-temperature electrolytes;[6] ultralow-temperature performance through tailored anion-solvent interactions in lithium metal batteries;[7] and synergistic cation–anion solvation engineering for reliable operation across extreme temperatures in high-voltage LIBs.[8] At the anode interphase, Azam *et al.*[9] demonstrated that high concentrations of vinylene carbonate (VC) effectively passivate graphite anode, suppress linear carbonate reduction and lithium alkoxide (LiOR) formation, and dramatically extend the lifetime of LFP/graphite pouch cells even at 70 °C. Building on this, Harlow *et al.*[10] further showed that a synergistic 2 wt% VC + 1 wt% 1,3,2-dioxathiolane 2,2-dioxide (DTD) additive blend forms robust, benign SEI and cathode-electrolyte interphase (CEI) layers capable of achieving LIB lifetimes exceeding two decades under aggressive conditions. More recently, Leslie *et al.*[11] reported that blended $LiPF_6$/LiFSI salts at reduced concentration significantly mitigate Mn deposition on graphite and improve the high-temperature stability of $LiMn_{0.8}Fe_{0.2}PO_4$/graphite cells by slowing Mn dissolution kinetics. Despite these advances, systematic studies elucidating the failure mechanisms of LMFP/graphite pouch cells, particularly the role of interphase composition in governing Mn dissolution, remain scarce.

In this work, we investigate the degradation pathways of $LiMn_{0.6}Fe_{0.4}PO_4$/graphite pouch cells by systematically comparing three electrolyte formulations: (1) a carbonate-based control electrolyte, (2) the control with 2 wt% VC, and (3) the control with 2 wt% VC + 1 wt% DTD. The $LiMn_{0.6}Fe_{0.4}PO_4$ composition was deliberately selected because it provides an optimal balance between higher operating voltage and structural stability, with partial Fe substitution stabilizing the olivine lattice while maintaining high Mn content for increased energy density. Using a combination of long-term cycling tests, electrochemical diagnostics, advanced X-ray spectroscopy, and density functional theory (DFT) calculations, we elucidate how electrolyte composition modulates CEI and SEI evolution and directly influences Mn dissolution behavior. Our results reveal that the VC + DTD synergistic additive package dramatically suppresses solvent decomposition and transition-metal leaching by forming resilient interphases on both electrodes. This study establishes an interphase-centric framework for understanding LMFP failure modes and demonstrates that targeted electrolyte engineering is a powerful, practical route to achieving ultra-long cycle life in high-energy-density, safe LMFP-based LIBs.

2. Experimental

Pouch cells and electrolyte preparation

Machine-fabricated 250 mAh $LiMn_{0.6}Fe_{0.4}PO_4$/graphite pouch cells without electrolyte (dry) were acquired by Lifun Technology (Hunan, China). The $LiMn_{0.6}Fe_{0.4}PO_4$ cathode active material was carbon-coated and contained 1.72 wt% carbon to enhance electronic conductivity. The cathode electrode consisted of 93 wt% carbon-coated $LiMn_{0.6}Fe_{0.4}PO_4$ active material, 2.6 wt% carbon black, and 4.4 wt% PVDF binder, while the graphite anode was composed of 95.7 wt% graphite active material, 3.0 wt% carboxymethyl cellulose/styrene–butadiene rubber (CMC/SBR) binder, and 1.3 wt% carbon black. The areal loadings of the cathode and anode were 13.53 mg cm^{-2} and 6.05 mg cm^{-2}, respectively. Copper foil served as the anode current collector, and aluminum foil as the cathode current collector, with an active electrode area of 146 cm^2. The separator was a 16 μm polyethylene (PE) membrane coated with a 4 μm ceramic layer. Electrolytes were prepared in an argon-filled glovebox (O_2 and H_2O < 0.01 ppm), using molality as the concentration unit. All electrolyte components were obtained from Shenzhen CapChem (China). The control (CTRL) electrolyte consisted of 1.2 m $LiPF_6$ (purity >99.0%) dissolved in a mixture of ethylene carbonate (EC), ethyl methyl carbonate (EMC), and dimethyl carbonate (DMC) in a 25 : 5 : 70 volume ratio. Additive-containing electrolytes were formulated by adding 2 wt% VC (H_2O < 20 ppm) to the CTRL electrolyte (denoted CTRL + 2VC) and subsequently incorporating 1 wt% DTD (H_2O < 20 ppm) into the CTRL + 2VC formulation to obtain CTRL + 2VC1DTD.

Formation and cycling

Pouch cells were filled with 1.0 g of electrolyte in an Ar-filled glovebox and vacuum-sealed using a compact vacuum sealer (MSK-115A-111, MTI Corp.) under a pressure of −90 kPa. The sealing process was conducted at 165 °C for 5 s. After electrolyte filling, the pouch cells were externally clamped to ensure

uniform pressure on the electrode stack and transferred to a temperature-controlled chamber (Neware Battery Testing System, Shenzhen, China) maintained at 40 ± 0.1 °C. A single formation cycle was performed on a Neware Battery Testing system (Shenzhen, China), where the cells were initially rested for 12 hours to ensure complete wetting. This was followed by a C/20 charge to 4.0 V, and a subsequent C/20 discharge to 1.5 V. After formation, the cells were degassed and re-sealed inside the argon-filled glovebox. Long-term cycling tests were then performed at 40 °C within a voltage window of 3–4.2 V. Cells were cycled under constant current-constant voltage (CCCV) charging and constant current (CC) discharging at a C/3 rate, with a C/10 cut-off current during the CV step. A C/20 check-up cycle was conducted every 50 cycles.

Gas volume measurement

The amount of gas generated in the pouch cells was determined through the application of Archimedes' principle, as detailed in the work by Aiken *et al.*[12]

Half-coin cells

To evaluate the specific capacity of the active materials, half-coin cells were prepared. Dry pouch cells were carefully opened, and the jelly roll was extracted and unrolled to separate the cathode and anode. Single-side coated electrodes were obtained by removing the electrode material from the current collectors using *N*-methyl-2-pyrrolidone (NMP) inside an Ar-filled glovebox.[13] Coin cell-sized electrodes (0.95 cm^2) were punched out and assembled into 2032-coin cells with Li metal as the counter electrode, a single polypropylene blown microfiber (BMF, 3M Co.) separator, and a 16 μm trilayer polypropylene-polyethylene-polypropylene (PP-PE-PP) membrane (Celgard). Approximately 100 μL of CTRL electrolyte was added to each cell. Half-coin cells were tested at 25 ± 0.1 °C in a temperature-controlled chamber. $LiMn_{0.6}Fe_{0.4}PO_4$/Li and graphite/Li cells were cycled at C/20 within voltage ranges of 3–4.3 V and 0.005–1.5 V, respectively.

Symmetric cells

Cathode and anode materials from after-formation and after-long-term-cycling pouch cells were carefully extracted and unrolled in an Ar-filled glovebox. Single-side coated electrodes were prepared using NMP, and coin cell-sized disks (0.95 cm^2) were punched out. Symmetric 2032-coin cells were assembled using the same electrolyte as in the parent pouch cells, with a single BMF separator and approximately 150 μL of electrolyte per cell. A detailed description of the symmetric cell assembly process can be found in Petibon *et al.*[14]

Electrochemical impedance spectroscopy (EIS) test

The EIS measurements were performed using a BioLogic VMP3 potentiostat. Each spectrum contained ten data points per decade within a frequency range of 100 kHz to 100 mHz, with a signal amplitude of 10 mV. Measurements were conducted at 10 °C, and each spectrum represents the average of two tests. The equivalent circuit models used for fitting are shown in Fig. S1, and all fittings were carried out using ZFit software (BioLogic). Both blocking and non-blocking electrodes were employed to differentiate the contributions of charge-transfer resistance (R_{ct}) and contact resistance ($R_{contact}$). At 0% state of charge (SOC), blocking electrodes prevent Li^+ intercalation into the electrode material, thereby suppressing faradaic reactions.[15–17] The $R_{contact}$ of the $LiMn_{0.6}Fe_{0.4}PO_4$ cathode and graphite anode were determined to be 4.53 Ω cm^2 and 14.05 Ω cm^2, respectively (Fig. S2).

Scanning electron microscopy (SEM)

SEM imaging was performed using a JEOL JSM-6480 microscope (JEOL, Japan) equipped with a tungsten (W) filament. The instrument was operated in secondary electron mode at an accelerating voltage of 20 kV.

X-ray diffraction (XRD)

XRD analysis was conducted using a Rigaku Miniflex Diffractometer equipped with Cu Kα radiation (wavelength of 1.5406 Å) over a 2θ range of 10–80° on fresh $LiMn_{0.6}Fe_{0.4}PO_4$ and graphite electrodes.

Soft X-ray absorption spectroscopy (Soft XAS)

Soft XAS measurements were conducted at the Stanford Synchrotron Radiation Light source (SSRL) on beamline 8-2 at a 55° incidence angle (magic angle) of X-ray incidence. The spectra were recorded using the 1000 lines per mm grating operated with 60*60 μm slits for the Ni L-edge data (~0.35 eV resolution). The spot size at the interaction point was around 1 × 1 mm^2 and the total flux was in the order of 10^{10} photons per s for which beam damage was not noticeable even for extended exposure. The data were collected both in the total electron yield (TEY) and fluorescence yield (FY) modes using the drain current (amplified by a Keithley picoammeter) for TEY and a Silicon Diode (IRD AXUV-1000) for FY. The incoming flux was recorded using a nickel grid with an Au sputtered film (i_0), collected in TEY, mounted upstream of the end station. Powder or electrode samples were loaded on carbon tape and then stuck to an aluminum sample holder. XAS samples were mounted on an aluminum holder with double-sided carbon tape in an Ar-filled glovebox and transferred to the load-lock chamber in a double-contained, argon-purged glove bag. Data was normalized using PyMCA software.

X-ray absorption spectroscopy (XAS)

XAS measurements for the Mn (6539 eV) and Fe (7112 eV) K-edges were performed at the 7-BM (QAS) beamline of the National Synchrotron Light Source II (Brookhaven National Laboratory, USA) in transmission mode. Mn and Fe metal foils were used as standard references to calibrate energy shifts. Reference compounds for transition metal oxidation states included $MnSO_4{\cdot}H_2O$ (purity >99%, Thermo Fisher Scientific), MnO_2 (purity >99.9%, Thermo Fisher Scientific), $FeSO_4{\cdot}7H_2O$ (purity >98%, Thermo Fisher Scientific), and Fe_2O_3 (purity >99.9%, Thermo Fisher Scientific). Each reference was mixed with sucrose ($C_{12}H_{22}O_{11}$) to achieve a 5 wt% metal content,

pelletized (0.1 g), and sealed in Kapton film to prevent air exposure. Three $LiMn_{0.6}Fe_{0.4}PO_4$/Li half-cells were charged to 3.65 and 4.2 V and discharged to 3.0 V (after charging to 4.2 V) *vs.* Li/Li^+ in CC(C/20)-CV(C/100) mode. The charged $LiMn_{0.6}Fe_{0.4}PO_4$ electrodes were then recovered from these half-coin cells in an Ar-filled glovebox, washed by DMC, dried, and sealed in Kapton film. Four spectra were collected for each K-edge and merged to improve the signal-to-noise ratio. The X-ray absorption near edge structure (XANES) spectra was analyzed using the Athena software package, with background, pre-edge, and post-edge lines defined for normalization. The extended X-ray absorption fine structure (EXAFS) spectra were Fourier transformed into the 3.0–13.7 $Å^{-1}$ *k*-range and fitted in the 1.0–4.5 Å *R*-range using Artemis. The fitting parameters included the passive electron reduction factor ($S_0{}^2$), Debye–Waller factor (σ^2), scattering distances (R), and ΔE_0. To simplify the model, only the core element was considered for calculating TM-O, TM-P, and TM-TM single scattering paths, as well as selected double scattering paths.

X-ray photoelectron spectroscopy (XPS)

Electrodes were extracted from pouch cells in an argon-filled glovebox, rinsed with anhydrous DMC, dried under vacuum in an antechamber overnight, and transferred to a PHI Versaprobe III *via* a sealed vacuum setup. XPS data were collected using a survey scan (pass energy 224 eV, step size 0.5 eV) and high-resolution scans (pass energy 25 eV, step size 0.05 eV), with surface neutralization achieved *via* low-energy Ar-ion flow and an electron neutralizer. The X-ray (25 W) was focused on a 100 μm spot. XPS spectra were fitted with SGL (50) line shapes on a Shirley background using CasaXPS software (v. 2.3.27PR4.8), with peaks adjusted to the C1*s* sp3 binding energy (284.8 eV) to correct for surface charging.

Micro-X-ray fluorescence (μXRF)

The graphite electrodes were extracted from the pouch cells after long-term cycling. Scanning μXRF measurements were conducted using a Bruker M4 Tornado μXRF system (Madison, WI, USA). All measurements were taken under a He atmosphere using a Rh X-ray tube, a 0–50 keV range and a 200 μA tube current. Sample scanning to obtain complete elemental analysis was done at a speed of 4.00 mm s^{-1} with a 25 μm spot size and either a 45 or 100 μm step size.

Density functional theory (DFT) calculation

All simulations in this study were carried out using the ABACUS open-source DFT software.[18–20] Within this software, we employed the semi-local Perdew–Burke–Ernzerhof (PBE)[21] functional, the localized atomic orbital (LCAO) basis set, and the Schlipf-Gygi norm-conserving pseudopotential.[22] In addition, the Grimme's DFTD3(BJ)[23] dispersion energy method was used to supplement necessary van der Waals (vdW) interactions, the DFT + U method[24] was used on transition metal (Fe and Mn with Hubbard U value 4.0 and 4.5 for d electrons[25]) species, and single-point implicit solvent energy correction[26] was added after the geometry relaxation of isolated complex system. Proper Gamma-centered k-grid settings were adjusted according to the unit cell sizes for energy convergence.

3. Results and discussion

The structure and morphology of cathode and anode electrode materials were characterized by XRD and SEM, respectively. Both electrodes were extracted from fresh dry pouch cells. The XRD pattern of the $LiMn_{0.6}Fe_{0.4}PO_4$ cathode (Fig. 1a) matched well with the standard $LiFePO_4$ diffraction pattern,[27] confirming an orthorhombic olivine structure with *Pmnb* (62) space group (JCPDS card number: 83-2092). A minor peak at ~27° arose from a carbon-related (002) reflection due to the conductive carbon black additive in the cathode formulation as well as the carbon-coating on the $LiMn_{0.6}Fe_{0.4}PO_4$ particle.[28,29] SEM analysis (Fig. 1b) revealed that the $LiMn_{0.6}Fe_{0.4}PO_4$ particles were uniformly distributed nanoparticles with an average diameter of approximately 100 nm. The XRD pattern of the graphite anode (Fig. S3a) displayed characteristic (002) and (004) reflections near 27° and 54°, respectively. Peaks corresponding to Cu (111), Cu (200), and Cu (220) at 43°, 51°, and 74° originated from the Cu current collector. SEM images of the graphite anode (Fig. S3b) showed flat particles with a broad size distribution ranging from 10 to 30 μm.

To examine the electrochemical behavior of these electrode materials, galvanostatic charge–discharge tests were conducted on $LiMn_{0.6}Fe_{0.4}PO_4$/Li and graphite/Li half-coin cells assembled with the CTRL electrolyte. Both electrodes were punched directly from the fresh pouch cells. The $LiMn_{0.6}Fe_{0.4}PO_4$/Li half-coin cells, cycled between 3 and 4.3 V (Fig. 1c), delivered a specific charge capacity of approximately 160 mAh g^{-1}, featuring two distinct voltage plateaus near 3.5 and 4.1 V, corresponding to the Fe^{2+}/Fe^{3+} and Mn^{2+}/Mn^{3+} redox couples, respectively.[2,3] The corresponding differential capacity (dQ/dV) plots (Fig. 1d) exhibited two pairs of peaks at similar potentials, consistent with the Li^+ intercalation/de-intercalation processes. Meanwhile, graphite/Li half-coin cells (Fig. S3c), cycled between 0.005 and 1.5 V, showed the typical graphite feature during lithiation/de-lithiation.

To understand the charge compensation mechanisms at different SOCs in $LiMn_{0.6}Fe_{0.4}PO_4$ cathode materials, *ex situ* XANES measurements were performed on fresh electrodes and those charged to 3.65 V, 4.2 V, and discharged back to 3.0 V during the first cycle at C/20 and 25 °C, along with reference compounds. The Fe K-edge spectra (Fig. 1e) showed that the main edge positions for samples charged to 3.65 V and 4.2 V closely matched that of Fe_2O_3, indicating that Fe predominantly existed as Fe^{3+} within this voltage range. The fresh $LiMn_{0.6}Fe_{0.4}PO_4$ electrode exhibited a main edge position consistent with $FeSO_4$, corresponding to Fe^{2+}, while a slight positive shift was observed upon discharge to 3.0 V, suggesting a partial increase in Fe valence. The Mn K-edge spectra (Fig. 1f) exhibited main edge positions similar to $MnSO_4$ for the fresh, 3.65 V charged, and 3.0 V discharged samples, confirming that

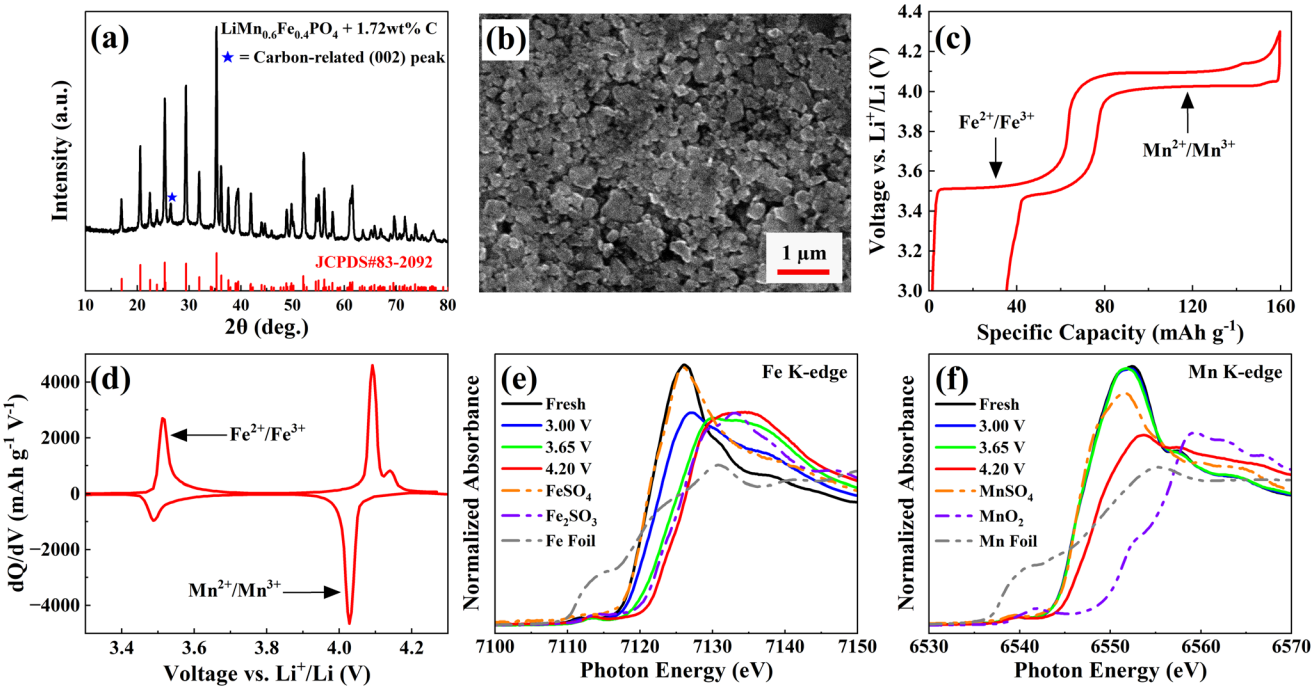

Fig. 1 Characterizations of $LiMn_{0.6}Fe_{0.4}PO_4$ cathode material. (a) XRD pattern and (b) SEM image of fresh $LiMn_{0.6}Fe_{0.4}PO_4$ electrode. (c) Voltage *vs.* specific capacity and (d) corresponding d*Q*/d*V vs.* voltage curves of $LiMn_{0.6}Fe_{0.4}PO_4$/Li half-coin cells cycled at C/20 and 25 °C. *Ex situ* XANES spectra of (e) Fe K-edge and (f) Mn K-edge in $LiMn_{0.6}Fe_{0.4}PO_4$ electrode at different voltages compared with reference samples.

Mn remained largely in the Mn^{2+} state up to 3.65 V. However, a noticeable shift toward higher energy was observed at 4.2 V, indicating partial oxidation of Mn^{2+} to Mn^{3+} at higher potential. These XANES results are consistent with the electrochemical data (Fig. 1c and d), confirming that Fe and Mn underwent sequential Fe^{2+}/Fe^{3+} and Mn^{2+}/Mn^{3+} redox reactions during charge and discharge.

Further insight into local structural changes was obtained from the corresponding *ex situ* EXAFS spectra at Fe and Mn K-edges, as shown in Fig. S4. The Fe K-edge EXAFS Fourier transformed spectra (Fig. S4a) revealed that the Fe–O, Fe–P, and Fe–TM bond lengths remained largely unchanged between the fresh and 3.0 V discharged samples. However, a distinct contraction of the Fe–O bond was observed upon charging to higher voltages, consistent with Fe oxidation (Tables S1–4). Similarly, the Mn K-edge EXAFS Fourier transformed spectra (Fig. S4b) showed that the Mn–O, Mn–P, and Mn–TM bond lengths were stable for the fresh, 3.65 V charged, and 3.0 V discharged electrodes, while splitting and decrease in intensity of the first Mn–O shell occurred upon charging to 4.2V. This behavior is typical for Jahn–Teller distortion, where shortening of some Mn–O bonds and lengthening of other Mn–O bonds distort [MnO_6] octahedra with increasing of repulsion between Mn and P (Tables S5–8).[30–32] These EXAFS findings further corroborate the XANES results, confirming the reversible Fe^{2+}/Fe^{3+} and Mn^{2+}/Mn^{3+} redox processes during electrochemical cycling.

Using $LiMn_{0.6}Fe_{0.4}PO_4$/graphite jelly-roll pouch cells (Fig. S5a) with N/P ratio of 1.23 (Fig. S5b), the effect of electrolyte formulation on cell failure mechanisms was evaluated. Three electrolyte formulations were selected including CTRL, CTRL + 2VC, and CTRL + 2VC1DTD. Formation process was conducted at 40 °C by charging the cells to 4.2 V at a C/20 current rate (Fig. 2a). The additive-containing electrolytes yielded higher first-cycle coulombic efficiencies (FCEs) of 89.1% for CTRL + 2VC and 89.3% for CTRL + 2VC1DTD, compared with 85.8% for the CTRL cell (Fig. S5c), indicating improved EEI during formation. The dQ/dV profiles during the early stage of the formation cycle (Fig. 2b) revealed the potential at which the additives were initially reduced on the surface of lithiated graphite to form the SEI. The CTRL cell exhibited a pronounced peak at ~2.8 V, corresponding to EC reduction on the graphite surface.[33,34] With 2% VC addition, this peak shifted to ~2.65 V, indicating VC reduction.[34,35] When 1% DTD was added alongside 2% VC, two distinct peaks appeared at ~2.4 V and ~2.65 V, corresponding to the reduction of DTD and VC.[35,36] These results indicate that both VC and DTD are reduced prior to EC, forming protective interphases that influence SEI composition and stability. Gas evolution, quantified using Archimedes' principle, was normalized by the cell's capacity (~250 mAh) as shown in Fig. 2c. The presence of VC significantly mitigated gas generation. The CTRL electrolyte produced the highest gas volume exceeding 7.34 mL Ah^{-1}, while CTRL + 2VC exhibited minimal gas evolution below 0.23 mL Ah^{-1}, and CTRL + 2VC1DTD showed a moderate amount of about 2.64 mL Ah^{-1}.

To further elucidate the electrochemical characteristics associated with these electrolyte formulations, EIS measure-

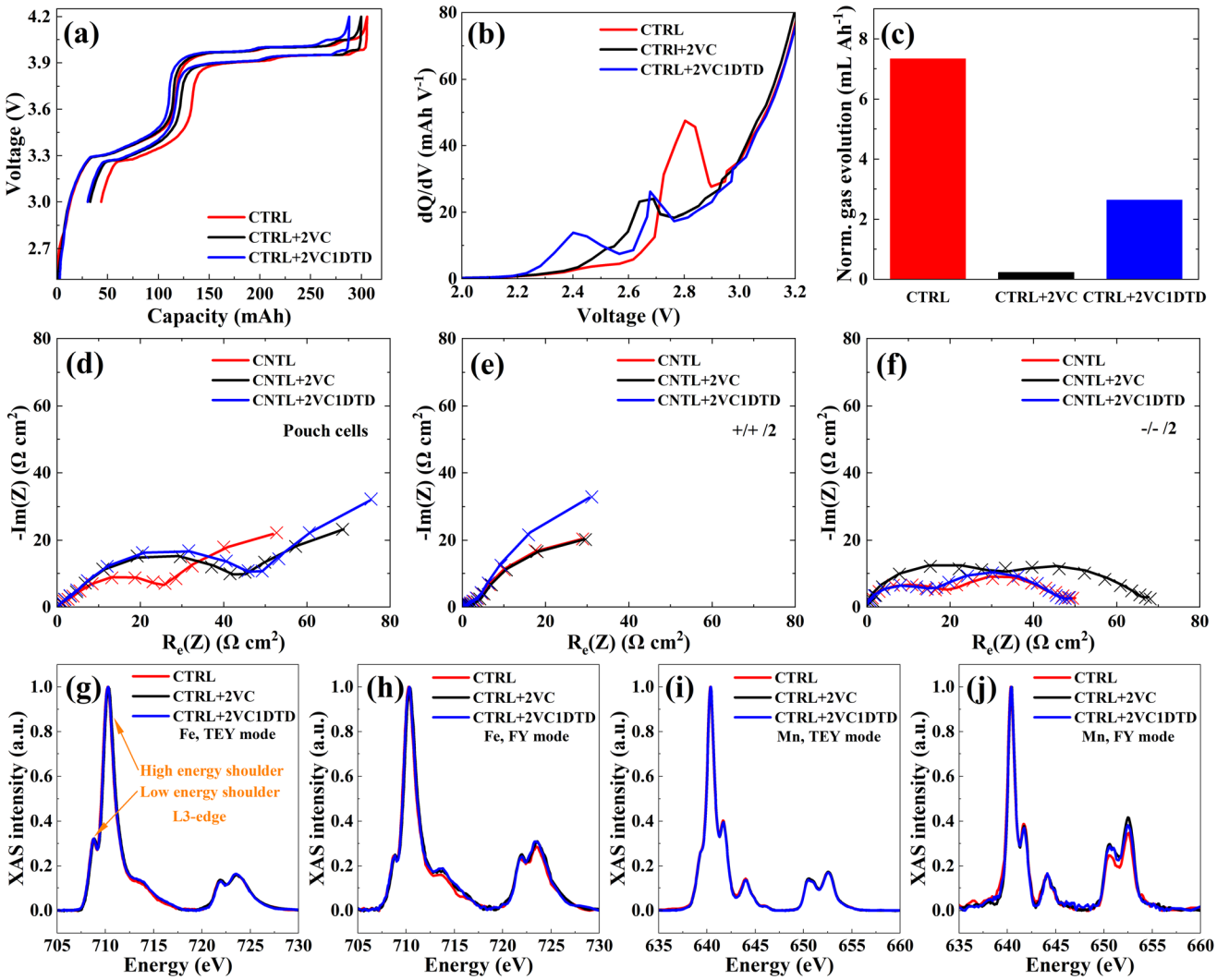

Fig. 2 Evaluation of the effects of electrolyte composition on the formation process of $LiMn_{0.6}Fe_{0.4}PO_4$/graphite pouch cells. (a) Voltage *vs.* capacity profiles, (b) d*Q*/d*V* *vs.* voltage curves during the early stages, and (c) capacity-normalized gas evolution of $LiMn_{0.6}Fe_{0.4}PO_4$/graphite pouch cells during formation. (d) Nyquist plot of the area specific impedance of $LiMn_{0.6}Fe_{0.4}PO_4$/graphite pouch cells at 3.9 V after cell formation. Nyquist plot of the area specific impedance of (e) $LiMn_{0.6}Fe_{0.4}PO_4$/$LiMn_{0.6}Fe_{0.4}PO_4$ and (f) graphite/graphite symmetric cells reconstructed from $LiMn_{0.6}Fe_{0.4}PO_4$/graphite pouch cells at 3.9 V after formation. All impedance measurements were performed at 10 °C. Experimental data are shown as solid line and fitted data are shown as cross symbols. Each spectrum is the average results of two cells measurement. Soft XAS spectra of $LiMn_{0.6}Fe_{0.4}PO_4$ cathode: Fe L-edge in (g) TEY and (h) FY mode, and Mn L-edge in (i) TEY and (j) FY mode, corresponding to (e).

ments were performed at 10 °C to evaluate charge-transfer resistance (R_{ct}, Fig. 2d–f). This parameter reflected the resistance to electrochemical reactions occurring at the EEI, where Li^+ or Li either gained or lost electrons to form neutral Li or reverted to Li^+, enabling their insertion into or extraction from the electrode material.[37,38] According to the Nyquist plots of the pouch cells (Fig. 2d) and equivalent circuit fitting (Table S9), cells containing electrolyte additives exhibited higher R_{ct} values than those with the CTRL electrolyte after formation. To determine whether the increase in R_{ct} originated primarily from the cathode or anode, EIS measurements with equivalent circuit fitting were performed on symmetric cells (Fig. 2e, f and Table S9). The results showed that adding 2 wt% VC primarily increases R_{ct} at the graphite anode side, whereas the combination of 2 wt% VC and 1 wt% DTD mainly increased R_{ct} at the $LiMn_{0.6}Fe_{0.4}PO_4$ cathode side. The CTRL electrolyte showed comparable R_{ct} values to CTRL + 2VC on the $LiMn_{0.6}Fe_{0.4}PO_4$ cathode side and to CTRL + 2VC1DTD on the graphite anode side.

The CEI was characterized using ensemble-averaged and surface-sensitive soft XAS. Fluorescence yield (FY) and total electron yield (TEY) modes were used to probe subsurface (50 nm) and surface (10 nm) chemical environments, respectively. Transition metal oxidation states were assessed based on the intensity ratio of the high- to low-energy shoulders in the L3-edge spectra, where a higher ratio corresponded to a higher oxidation state.[39,40] Comparison of FY and TEY spectra revealed depth-dependent chemical variations influenced by

electrolyte composition during formation. The results showed no significant differences in Fe oxidation states among the electrolytes in either TEY or FY modes (Fig. 2g and h), and a similar trend was observed for the Mn oxidation states in both TEY and FY modes (Fig. 2i and j).

To evaluate the influence of electrolyte formulation on the cycling lifespan of $LiMn_{0.6}Fe_{0.4}PO_4$/graphite pouch cells, cells were cycled at a C/3 rate in CCCV mode with a C/10 cut-off current, between 3 and 4.2 V at 40 °C, with periodic C/20 check-up cycles every 50 cycles. Fig. 3a showed the discharge capacity and coulombic efficiency (CE) as a function of cycle number, while Fig. 3b showed the discharge capacities normalized to the first C/3 discharge *vs.* cycler numbers. The CTRL cell exhibited the poorest cycling performance, retaining only ~80% of its initial capacity after 165 cycles. In contrast, the addition of 2 wt% VC markedly improved performance, with the CTRL + 2VC cell maintaining ~87% capacity after 390 cycles. The CTRL + 2VC1DTD cell demonstrated the best performance, retaining ~85% of its capacity even after 610 cycles. The delta V (Fig. 3c) is the difference between the average charge and the average discharge voltage, which indicates voltage polarization growth during cycling. Both additive-containing cells displayed gradual, modest increases in delta V during cycling, with the CTRL + 2VC1DTD cell showing the most stable behavior. Consistent with these trends, gas evolution measurements (Fig. 3d) revealed that the CTRL cell produced the largest gas volume (~2 mL Ah^{-1}) during extended cycling, while cells containing additives generated significantly less gas (~0.5 mL Ah^{-1}). These results collectively indicated that selected electrolyte additives effectively suppressed interphasial degradation, mitigate gas evolution, and improve long-term cycling stability of $LiMn_{0.6}Fe_{0.4}PO_4$/graphite pouch cells.

To investigate failure mechanisms in cells with different electrolyte formulations, an in-depth analysis of electrode morphology, chemical composition, and EEI evolution was conducted using SEM, EIS with equivalent circuit analysis, soft XAS, and μXRF. Electrode samples were harvested from cycled cells inside a glovebox to prevent air exposure. The $LiMn_{0.6}Fe_{0.4}PO_4$ cathodes from the CTRL, CTRL + 2VC, and CTRL + 2VC1DTD cells (Fig. S6a–c) exhibited similar morphologies across all electrolyte formulations, as did the graphite anodes (Fig. S6d–f).

EIS measurements combined with equivalent circuit fitting were conducted to track changes in R_{ct} values during long-term cycling (Fig. 4a–c and Table S10). According to the Nyquist plots of the pouch cells (Fig. 4a) and equivalent circuit fitting (Table S10), all cells exhibited an increase in R_{ct} values of ~100 Ω cm^2. To unravel the source of impedance growth,

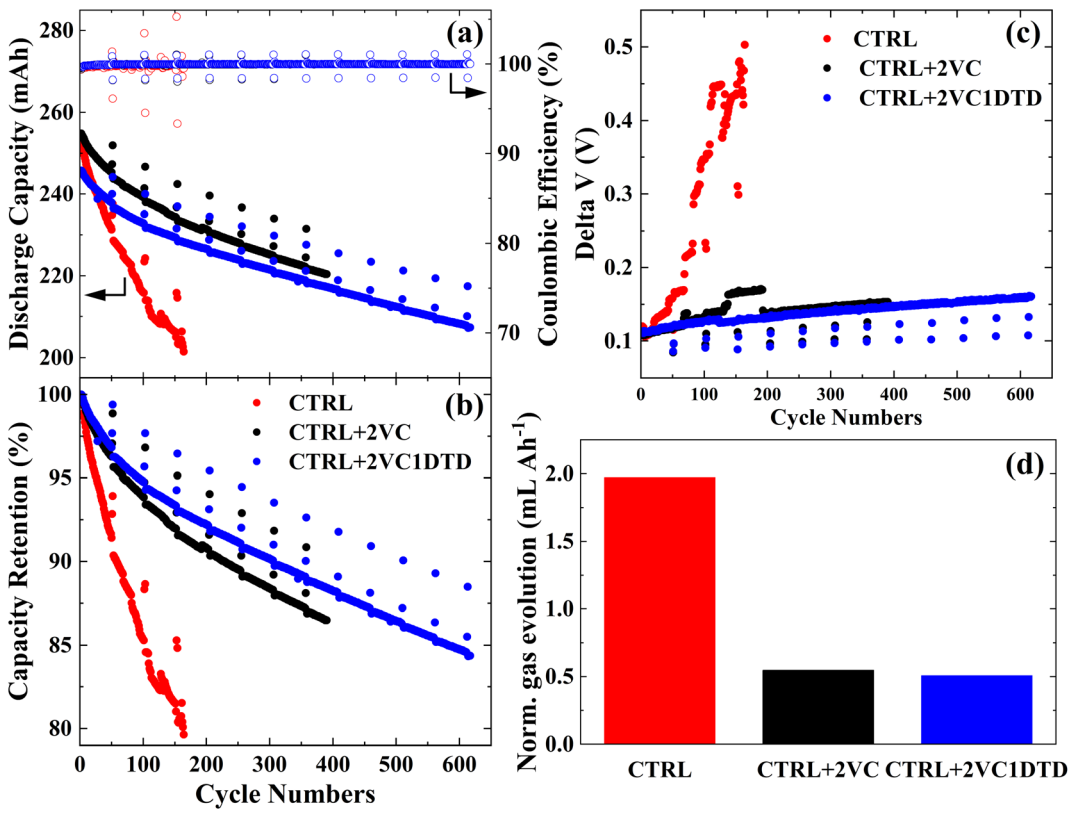

Fig. 3 Evaluation of electrochemical performance of $LiMn_{0.6}Fe_{0.4}PO_4$/graphite pouch cells with three electrolytes: 1.2 m $LiPF_6$ in EC : EMC : DMC (25 : 5 : 70 by vol.) (CTRL), CTRL + 2% VC, and CTRL + 2% VC + 1% DTD. (a) discharge capacity, (b) capacity retention, (c) delta V *vs.* cycling numbers during long-term cycling between 3 and 4.2 V at 40 °C with a rate of C/3 in CCCV mode with a C/10 cut-off current. A cycle of C/20 was performed every 50 cycles. (d) Capacity-normalized gas evolution of $LiMn_{0.6}Fe_{0.4}PO_4$/graphite pouch cells after long-term cycling.

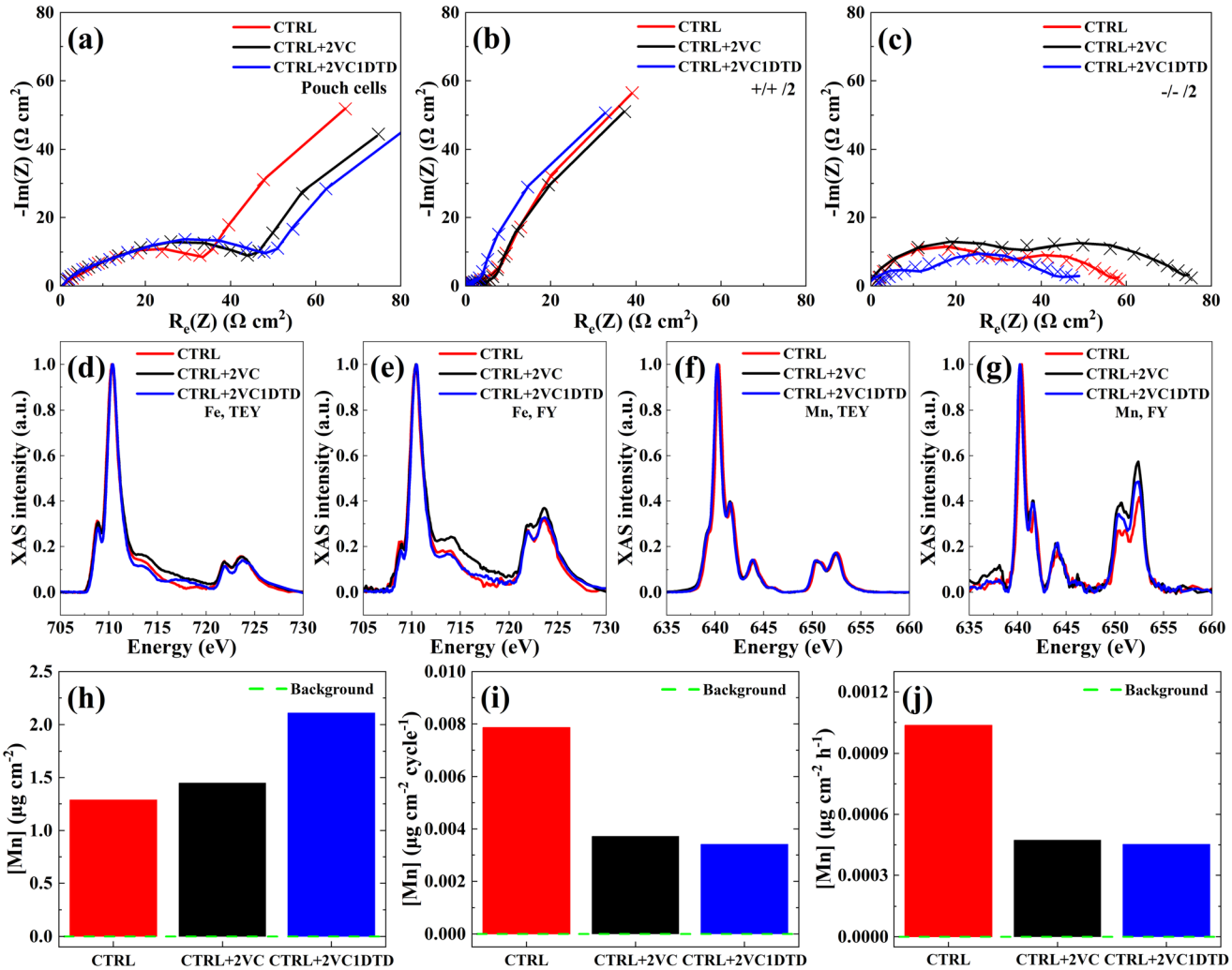

Fig. 4 Analysis of failure mechanisms in $LiMn_{0.6}Fe_{0.4}PO_4$/graphite pouch cells after long-term cycling. (a) Nyquist plot of the area specific impedance of $LiMn_{0.6}Fe_{0.4}PO_4$/graphite pouch cells at 3.9 V after long-term cycling. Nyquist plot of the area specific impedance of (b) $LiMn_{0.6}Fe_{0.4}PO_4$/$LiMn_{0.6}Fe_{0.4}PO_4$ and (c) graphite/graphite symmetric cells reconstructed from $LiMn_{0.6}Fe_{0.4}PO_4$/graphite pouch cells at 3.9 V after long-term cycling. All impedance measurements were performed at 10 °C. Experimental data are shown as solid line and fitted data are shown as cross symbols. Each spectrum is the average results of two cells measurement. Soft XAS spectra of $LiMn_{0.6}Fe_{0.4}PO_4$ cathode: Fe L-edge in (d) TEY and (e) FY mode, and Mn L-edge in (f) TEY and (g) FY mode, corresponding to (b). (h) Total Mn deposition, (i) the Mn deposition rate per cycle, (j) the Mn deposition rate per hour measured by μXRF on the graphite electrode after long-term cycling. The green dashed line shows the Mn baseline on a fresh graphite electrode.

symmetric cells were constructed to analyze the changes in R_{ct} values at both $LiMn_{0.6}Fe_{0.4}PO_4$ cathode (Fig. 4b) and graphite anode (Fig. 4c). The majority of the R_{ct} originated from the $LiMn_{0.6}Fe_{0.4}PO_4$ cathode, while the graphite anode contributed only about ~10 Ω cm^2 (Table S10). Because the cells reached different cycle numbers, the R_{ct} values were normalized by cycle numbers to allow fair comparison. After normalization by cycle number (Fig. S7a and Table S11) showed that the cathode exhibited normalized R_{ct} growth rates of 0.6534, 0.2274, and 0.17 Ω cm^2 per cycle for the CTRL, CTRL + 2VC, and CTRL + 2VC1DTD cells, respectively. These values are approximately 8–12 times higher than the corresponding anode contributions (0.0696, 0.02375, and 0.0092 Ω cm^2 per cycle), unambiguously demonstrating that impedance growth is overwhelmingly dominated by degradation processes at the $LiMn_{0.6}Fe_{0.4}PO_4$ cathode. Moreover, the normalized results revealed that the CTRL cell exhibited the fastest rate of impedance growth, while the CTRL + 2VC1DTD cell showed the slowest, demonstrating electrolyte additives, particularly the combination of VC and DTD, effectively mitigated interphasial degradation during extended cycling.

To further elucidate how the electrolyte formulations influenced the impedance evolution rate at the $LiMn_{0.6}Fe_{0.4}PO_4$ cathode, the CEI post-cycling was examined using the soft XAS employing TEY and FY modes at the Fe and Mn L-edges. The TEY and FY data highlighted variations in chemical composition with depth, especially for electrochemically active species including Fe and Mn, impacted by the electrolyte for-

mulations. For both Fe and Mn, a higher intensity ratio of the high- to low-energy shoulders in the L3-edge spectra corresponded to a higher oxidation state, where reduction typically reflects electrolyte oxidation processes. As shown in Fig. 4d and e, the Fe L3-edge spectra exhibited small differences among the electrolyte formulations in both TEY and FY modes. The addition of 2 wt% VC led to a slightly higher Fe oxidation state, while the combination of 2 wt% VC and 1 wt% DTD produced the highest oxidation state in both modes (Fig. S7b). In contrast, the CTRL electrolyte showed the lowest oxidation state. Notably, the FY mode consistently indicated higher Fe oxidation states than the TEY mode for all samples, suggesting an oxidation-state gradient that increased from the surface toward the subsurface region. For Mn, minimal changes in the L3-edge spectra were observed among the electrolyte formulations in the TEY mode (Fig. 4f), whereas small variations were evident in the FY mode (Fig. 4g). The surface Mn oxidation states appeared similar for all electrolytes, but in the subsurface region (FY mode), the CTRL sample exhibited a slightly lower oxidation state compared with the additive-containing electrolytes (Fig. S7c). Overall, the Mn oxidation states obtained from TEY and FY modes were comparable, indicating that no significant oxidation-state gradient existed between the surface and subsurface regions.

The dominant degradation mechanism of LMFP-based cells was the rapid loss of Li inventory, catalyzed by Mn dissolution from the LMFP cathode and subsequent deposition on the graphite anode.[41] Dissolved Mn species migrated to the graphite anode and incorporated into the SEI.[42] This incorporation destabilized the SEI, leading to its continual breakdown and reformation, which consumed active Li inventory and accelerated capacity fading.[11] Reducing the rate of Mn dissolution and deposition on the graphite anode was therefore critical to extending the lifespan of LMFP-based cells. Fig. 4h–j showed the quantified Mn loadings obtained by μXRF analysis. The total Mn loading (Fig. 4h) was the lowest for the CTRL cell, whereas the CTRL + 2VC1DTD cell exhibited the highest value, with the CTRL + 2VC cell slightly exceeding the CTRL cell. To account for the different cycling durations, Mn deposition was normalized by cycle number and total cycling time. As shown in Fig. 4i and j, the CTRL cell exhibited nearly twice the Mn dissolution rate compared with the additive-containing cells, while the CTRL + 2VC cell showed a slightly higher rate than the CTRL + 2VC1DTD cell. These results confirm that the inclusion of VC and DTD additives effectively suppressed Mn dissolution and mitigated lithium inventory loss during extended cycling. Additionally, Fe was not detected on the graphite anode, consistent with previous reports.[11,41] This selective Mn dissolution, with negligible Fe dissolution, was characteristic of LMFP cathodes and arose from the pronounced Jahn–Teller distortion of Mn^{3+}, which destabilized the lattice and facilitated Mn^{2+} release. In contrast, the Fe^{2+}/Fe^{3+} redox couple induced minimal structural strain and remained strongly coordinated within the olivine lattice, resulting in much lower solubility in carbonate electrolytes. Consequently, transition-metal dissolution in LMFP-based cells is overwhelmingly Mn-driven rather than Fe-driven.

Although Mn dissolution is well recognized as the primary degradation mechanism in LMFP-based cells,[11,41] the atomic-level pathway governing Mn release remains poorly understood. Recent studies have implicated LiOR, formed *via* reductive decomposition of linear carbonate solvents, as key species responsible for transition-metal dissolution from oxide and polyanion cathodes.[9,43,44] In the present electrolyte solvents (*i.e.*, 70 vol% DMC + 5 vol% EMC), DMC reduction is the primary source of lithium methoxide (MeOLi),[45–47] whereas EMC predominantly undergoes transesterification to yield DMC and diethyl carbonate (DEC).[48,49] Cycling-induced evolution of SEI chemistries, as revealed by *ex situ* XPS (Fig. S8 and Table S12), further indicates this ongoing carbonate reduction and the accumulation of alkoxide species. It should be noted that Mn-related degradation is expected to be kinetically suppressed at lower temperatures, where performance is limited primarily by graphite anode kinetics and Li^+ transport rather than cathode dissolution. To elucidate whether MeOLi can thermodynamically drive Mn extraction from the LMFP lattice, DFT calculations were performed using MeOLi as a representative alkoxide model.

Li^+ diffusion in LMFP cathode materials occurred primarily along the [010] (*b* axis) direction.[50,51] To model this structure, a $LiMn_{0.6}Fe_{0.4}PO_4$ bulk structure without partial atom occupation was first constructed by expanding the unit cell obtained from X-ray diffraction[50] fivefold along the (*a*, *c*) lattice plane (Fig. S9a). After full relaxation, this bulk model was used to build 2D slab models with (010) lattice plane exposed as the surface. Four distinct (010) surface terminations were created while preserving stoichiometry: two with unsaturated Li or Mn/Fe cations on the surface and two with saturated metal atoms and dangling O on the surface (named as Li-top, Mn/Fe-top, Li–O-top, and Mn/Fe–O-top, shown in Fig. S9b–e). Total energy analysis (Table S13) revealed that the Mn/Fe-top surface possessed the lowest total energy, indicating it to be the most stable configuration and thus, the most representative active surface for subsequent reactivity studies. To investigate the influence of MeOLi on metal dissolution from LMFP-based cathode, the Mn/Fe-top (010) surface with different MeOLi ligand poses were enumerated (Fig. 5). Three adsorption configurations (Pose 1–3) were optimized, yielding total energies of −102 221.483 eV, −102 222.284 eV, and −102 222.007 eV, respectively. Among these, Pose 2 exhibited the lowest total energy, indicating the most stable configuration for MeOLi adsorption on the surface. This configuration was subsequently used to model the structure with surface Mn^{2+} removal (marked with an asterisk). After relaxation, the slab system with one Mn^{2+} loss (at different sites) and two Li^+ gain showed total energies of −98 237.532 eV and −98 236.009 eV, while the isolated manganese methoxide ($Mn(MeO)_2$) complex exhibited an energy of −3981.171 eV. These computed energy values indicate that the MeOLi-assisted surface Mn^{2+} dissolution requires at least 3.58 eV of energy. This indicates the nucleophilic alkoxide species, such as MeOLi generated during electrolyte reduction at the graphite anode, can potentially interact with surface Mn sites at the LMFP cathode,

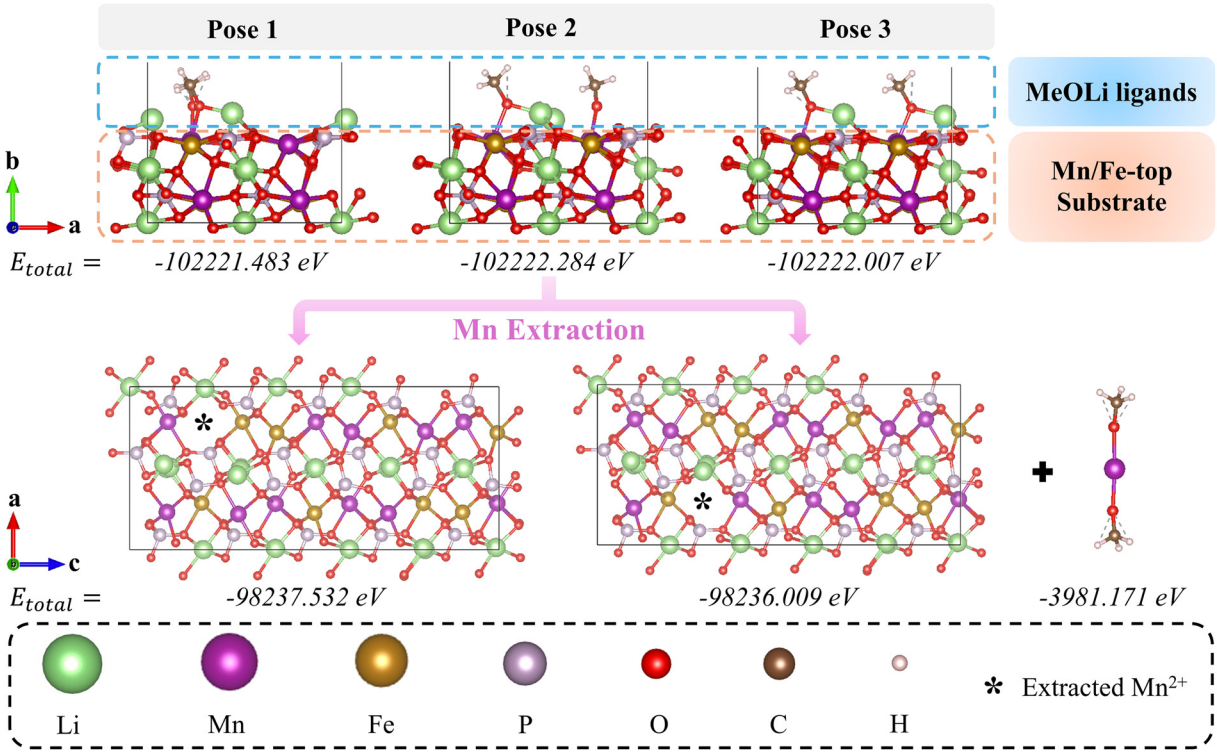

Fig. 5 MeOLi-assisted Mn^{2+} dissolution process investigated by DFT. Three types of MeOLi attaching configurations on the $LiMn_{0.6}Fe_{0.4}PO_4$ cathode surface were enumerated. Afterwards, Mn^{2+} from two different types of sites were extracted from the surface together with the MeO^- anions, forming $Mn(MeO)_2$.

thereby facilitating Mn dissolution. The atomistic insights obtained from the DFT calculations provided us an energetic understanding of the experimentally observed Mn dissolution and highlight the critical role of electrolyte decomposition products in accelerating capacity fading in LMFP-based lithium-ion cells.

4. Conclusion

This work provides a comprehensive understanding of the electrochemical stability and degradation mechanisms in $LiMn_{0.6}Fe_{0.4}PO_4$/graphite pouch cells by systematically evaluating three electrolyte formulations including control carbonate electrolyte, control + 2 wt% VC, and control + 2 wt% VC + 1 wt% DTD. Through integrated electrochemical testing, symmetric-cell impedance analysis, advanced X-ray spectroscopies, and DFT calculations, we establish an interphase-centered framework that explains how electrolyte composition dictates long-term performance and failure.

During formation, both VC and DTD additives are preferentially reduced prior to EC, generating more stable CEI and SEI layers, suppressing gas evolution, and increasing first-cycle coulombic efficiency to 89.3%. Long-term cycling at 40 °C demonstrates that the synergistic VC + DTD electrolyte produces the most robust interphases, resulting in minimized impedance growth and markedly improved performance, retaining over 85% of its initial capacity after 600 cycles at C/3. In contrast, the control electrolyte exhibits rapid CEI/SEI degradation, severe Mn dissolution, and accelerated interphasial impedance growth, collectively driving early cell failure.

Post-mortem spectroscopic analyses corroborate these electrochemical trends. Soft XAS reveals that the VC + DTD combination effectively suppresses electrolyte oxidation at the $LiMn_{0.6}Fe_{0.4}PO_4$ cathode, while μXRF confirms substantially reduced Mn dissolution relative to the control electrolyte. Together, these findings confirm that such degradation processes were the primary contributors to lithium inventory loss. Additionally, DFT calculations provide atomistic and energetic insights into the Mn-dissolution mechanism, demonstrating that lithium alkoxide species, for example MeOLi, generated from solvent reduction at imperfectly passivated graphite surfaces act as nucleophilic species that facilitate Mn^{2+} extraction. This mechanistic connection between LiOR formation, interphase breakdown, and transition-metal dissolution explains the degradation pathways in LMFP/graphite cells.

Overall, this study provides mechanistic insight into LMFP/graphite cell degradation and demonstrates that the synergistic use of VC and DTD effectively stabilizes both the CEI and SEI, thereby mitigating electrolyte decomposition, Mn dissolution, and LiOR formation. By directly linking electrolyte decomposition pathways to interphase evolution, this work establishes an interphase-centric framework for understanding failure mechanisms in LMFP-based pouch cells and clarifies why the

dual-additive electrolyte most effectively suppresses the dominant degradation processes. These insights highlight the central role of interphase engineering in enabling long-life LMFP-based batteries and provide guiding principles for the rational design of future electrolyte formulations aimed at further suppressing Mn dissolution and enhancing interphasial robustness.

Conflicts of interest

There are no conflicts to declare.

Data availability

The data supporting the findings of this study are available from the corresponding author upon reasonable request. Supplementary information (SI) is available. See DOI: https://doi.org/10.1039/d5eb00228a.

Acknowledgements

Lin Ma acknowledges the support of the start-up fund from UNC Chapel Hill. This research used 7-BM (QAS) beamline of the National Synchrotron Light Source II, a U.S. Department of Energy (DOE) Office of Science User Facility operated for the DOE Office of Science by Brookhaven National Laboratory under Contract No. DE-SC0012704. The authors also acknowledge the use of Beamline 8-2 with assistance from Dr Dennis Nordlund at the Stanford Synchrotron Radiation Light source, SLAC National Accelerator Laboratory, which was supported by the U.S. Department of Energy, Office of Science, Office of Basic Energy Sciences under Contract no. DE-AC02-76SF00515.

References

1 M. M. Hasan, R. Haque, M. I. Jahirul, M. G. Rasul, I. M. R. Fattah, N. M. S. Hassan and M. Mofijur, Advancing energy storage: The future trajectory of lithium-ion battery technologies, *J. Energy Storage*, 2025, **120**, 116511.
2 A. K. Padhi, K. S. Nanjundaswamy and J. B. Goodenough, Phospho–olivines as Positive–Electrode Materials for Rechargeable Lithium Batteries, *J. Electrochem. Soc.*, 1997, **144**(4), 1188.
3 A. Yamada and S.-C. Chung, Crystal Chemistry of the Olivine-Type Li (Mny Fe_{1-y}) PO_4 and $(Mn_yFe_{1-y})PO_4$ as Possible 4 V Cathode Materials for Lithium Batteries, *J. Electrochem. Soc.*, 2001, **148**(8), A960.
4 C. Chak, V. Shipitsyn and L. Ma, Thermal Stability Comparison of $LiFePO_4$/Graphite and $LiMn_{0.6}Fe_{0.4}PO_4$/Graphite Pouch Cells using Accelerating Rate Calorimetry, *J. Electrochem. Soc.*, 2025, **172**(9), 090532.
5 T. Liu, A. Dai, J. Lu, Y. Yuan, Y. Xiao, L. Yu, M. Li, J. Gim, L. Ma and J. Liu, Correlation between manganese dissolution and dynamic phase stability in spinel-based lithium-ion battery, *Nat. Commun.*, 2019, **10**(1), 4721.
6 N. Zhang, A.-M. Li, W. Zhang, Z. Wang, Y. Liu, X. Zhang, G. Cai, H. Wan, J. Xu and C. Wang, 4.6 V Moisture-Tolerant Electrolytes for Lithium-Ion Batteries, *Adv. Mater.*, 2024, **36**(50), 2408039.
7 J. Xu, V. Koverga, A. Phan, A. min Li, N. Zhang, M. Baek, C. Jayawardana, B. L. Lucht, A. T. Ngo and C. Wang, Revealing the Anion–Solvent Interaction for Ultralow Temperature Lithium Metal Batteries, *Adv. Mater.*, 2024, **36**(7), 2306462.
8 H. Zhang, Y. Zhao, X. Li, H. Wang, L. Wang, Y. Song, F. Qiao, J. Wang and J. Xu, Wide-Temperature Electrolyte Design via Cation-Anion Solvation Engineering for 4.6 V Lithium-Ion Batteries, *Adv. Sci.*, 2025, **12**(32), e03151.
9 S. Azam, W. Black, H. MacLennan, A. Adamson, E. Zsoldos, E. R. Logan and J. R. Dahn, Improving and Understanding Lifetime of LFP/Graphite Pouch Cells with Higher Concentrations of Vinylene Carbonate in the Electrolyte, *J. Electrochem. Soc.*, 2025, **172**(7), 070523.
10 J. E. Harlow, X. Ma, J. Li, E. Logan, Y. Liu, N. Zhang, L. Ma, S. L. Glazier, M. M. Cormier and M. Genovese, A wide range of testing results on an excellent lithium-ion cell chemistry to be used as benchmarks for new battery technologies, *J. Electrochem. Soc.*, 2019, **166**(13), A3031.
11 K. Leslie, J. J. Abraham, H. MacLennan, R. Fenner, J. R. Dahn and M. Metzger, Reducing the Rate of Mn Dissolution in $LiMn_{0.8}Fe_{0.2}PO_4$/Graphite Cells with Mixed Salt and Low Salt Molarity Electrolytes, *J. Electrochem. Soc.*, 2025, **172**(4), 040515.
12 C. P. Aiken, J. Xia, D. Y. Wang, D. A. Stevens, S. Trussler and J. R. Dahn, An Apparatus for the Study of In Situ Gas Evolution in Li-Ion Pouch Cells, *J. Electrochem. Soc.*, 2014, **161**(10), A1548.
13 R. Jayakumar, T. P. Pollard, O. Borodin, V. Shipitsyn, C. Chak, G. Pastel, A. Zheng, M. Johnson, F. Hasan, C. M. Bejger, M. A. Schroeder, S. G. Greenbaum, W. Zuo and L. Ma, Weakly solvating ester electrolyte for high voltage sodium-ion batteries, *Nano Energy*, 2024, **128**, 109969.
14 R. Petibon, C. P. Aiken, N. N. Sinha, J. C. Burns, H. Ye, C. M. VanElzen, G. Jain, S. Trussler and J. R. Dahn, Study of Electrolyte Additives Using Electrochemical Impedance Spectroscopy on Symmetric Cells, *J. Electrochem. Soc.*, 2013, **160**(1), A117.
15 J. Landesfeind, J. Hattendorff, A. Ehrl, W. A. Wall and H. A. Gasteiger, Tortuosity Determination of Battery Electrodes and Separators by Impedance Spectroscopy, *J. Electrochem. Soc.*, 2016, **163**(7), A1373.
16 A. S. Keefe, S. Buteau, I. G. Hill and J. R. Dahn, Temperature Dependent EIS Studies Separating Charge Transfer Impedance from Contact Impedance in Lithium-Ion Symmetric Cells, *J. Electrochem. Soc.*, 2019, **166**(14), A3272.
17 C. Chak, V. Shipitsyn and L. Ma, Cathode-Anode Interactions in Layered Oxide/Sn Alloy Sodium-Ion Pouch Cells at High Temperature and Voltage, *ECS Adv.*, 2025, **4**(4), 040502.

18 M. Chen, G. C. Guo and L. He, Systematically improvable optimized atomic basis sets for ab initio calculations, *J. Phys.: Condens. Matter*, 2010, **22**(44), 445501.
19 P. Li, X. Liu, M. Chen, P. Lin, X. Ren, L. Lin, C. Yang and L. He, Large-scale ab initio simulations based on systematically improvable atomic basis, *Comput. Mater. Sci.*, 2016, **112**, 503–517.
20 P. Lin, X. Ren, X. Liu and L. He, Ab initio electronic structure calculations based on numerical atomic orbitals: Basic fomalisms and recent progresses, *Wiley Interdiscip. Rev.: Comput. Mol. Sci.*, 2024, **14**(1), e1687.
21 J. P. Perdew, K. Burke and M. Ernzerhof, Generalized Gradient Approximation Made Simple, *Phys. Rev. Lett.*, 1996, **77**(18), 3865–3868.
22 M. Schlipf and F. Gygi, Optimization algorithm for the generation of ONCV pseudopotentials, *Comput. Phys. Commun.*, 2015, **196**, 36–44.
23 S. Grimme, S. Ehrlich and L. Goerigk, Effect of the damping function in dispersion corrected density functional theory, *J. Comput. Chem.*, 2011, **32**(7), 1456–1465.
24 X. Qu, P. Xu, H. Jiang, L. He and X. Ren, DFT + U within the framework of linear combination of numerical atomic orbitals, *J. Chem. Phys.*, 2022, **156**(23), 234104.
25 H. Guo, R. Liu, W. Li, H. Gu, J. Cao, D. Gong and G. Liang, Site Selection of Niobium-Doped $LiMn_{0.6}Fe_{0.4}PO_4$ and Effect on Electrochemical Properties, *J. Electrochem. Soc.*, 2023, **170**(3), 030542.
26 D. S. Hall, J. Self and J. R. Dahn, Dielectric Constants for Quantum Chemistry and Li-Ion Batteries: Solvent Blends of Ethylene Carbonate and Ethyl Methyl Carbonate, *J. Phys. Chem. C*, 2015, **119**(39), 22322–22330.
27 J. Hou, L. Wang, X. Feng, J. Terada, L. Lu, S. Yamazaki, A. Su, Y. Kuwajima, Y. Chen, T. Hidaka, X. He, H. Wang and M. Ouyang, Thermal Runaway of Lithium-Ion Batteries Employing Flame-Retardant Fluorinated Electrolytes, *Energy Environ. Mater.*, 2023, **6**(1), e12297.
28 V. Shipitsyn, R. Jayakumar, W. Zuo, W. Yin, E. Huber and L. Ma, The Impact of Fluoroethylene Carbonate Additive on Charged Sodium Ion Electrodes/Electrolyte Reactivity Studied Using Accelerating Rate Calorimetry, *J. Electrochem. Soc.*, 2023, **170**(11), 110501.
29 T. Ungár, J. Gubicza, G. Ribárik, C. Pantea and T. W. Zerda, Microstructure of carbon blacks determined by X-ray diffraction profile analysis, *Carbon*, 2002, **40**(6), 929–937.
30 D.-H. Seo, H. Gwon, S.-W. Kim, J. Kim and K. Kang, Multicomponent Olivine Cathode for Lithium Rechargeable Batteries: A First-Principles Study, *Chem. Mater.*, 2010, **22**(2), 518–523.
31 L. F. J. Piper, N. F. Quackenbush, S. Sallis, D. O. Scanlon, G. W. Watson, K. W. Nam, X. Q. Yang, K. E. Smith, F. Omenya, N. A. Chernova and M. S. Whittingham, Elucidating the Nature of Pseudo Jahn–Teller Distortions in Li_xMnPO_4: Combining Density Functional Theory with Soft and Hard X-ray Spectroscopy, *J. Phys. Chem. C*, 2013, **117**(20), 10383–10396.
32 S. Wi, J. Park, S. Lee, J. Kang, T. Hwang, K.-S. Lee, H.-K. Lee, S. Nam, C. Kim, Y.-E. Sung and B. Park, Synchrotron-based X-ray absorption spectroscopy for the electronic structure of $Li_xMn_{0.8}Fe_{0.2}PO_4$ mesocrystal in Li+ batteries, *Nano Energy*, 2017, **31**, 495–503.
33 Y. Domi, M. Ochida, S. Tsubouchi, H. Nakagawa, T. Yamanaka, T. Doi, T. Abe and Z. Ogumi, In Situ AFM Study of Surface Film Formation on the Edge Plane of HOPG for Lithium-Ion Batteries, *J. Phys. Chem. C*, 2011, **115**(51), 25484–25489.
34 J. Xia, L. Ma, C. P. Aiken, K. J. Nelson, L. P. Chen and J. R. Dahn, Comparative Study on Prop-1-ene-1,3-sultone and Vinylene Carbonate as Electrolyte Additives for Li $(Ni_{1/3}Mn_{13}Co_{1/3})O_2$/Graphite Pouch Cells, *J. Electrochem. Soc.*, 2014, **161**(10), A1634.
35 J. Xia, N. N. Sinha, L. P. Chen and J. R. Dahn, A Comparative Study of a Family of Sulfate Electrolyte Additives, *J. Electrochem. Soc.*, 2014, **161**(3), A264.
36 D. S. Hall, J. P. Allen, S. L. Glazier, L. D. Ellis, L. Ma, J. M. Peters, I. G. Hill and J. R. Dahn, The Solid-Electrolyte Interphase Formation Reactions of Ethylene Sulfate and Its Synergistic Chemistry with Prop-1-ene-1,3-Sultone in Lithium-Ion Cells, *J. Electrochem. Soc.*, 2017, **164**(14), A3445.
37 A. J. Bard, L. R. Faulkner and H. S. White, *Electrochemical methods: fundamentals and applications*, John Wiley & Sons, 2022.
38 Q.-C. Zhuang, X.-Y. Qiu, S.-D. Xu, Y.-H. Qiang and S. Su, Diagnosis of electrochemical impedance spectroscopy in lithium-ion batteries, *Lithium Ion Batteries: New Dev.*, 2012, **8**, 189–227.
39 L. Mu, X. Feng, R. Kou, Y. Zhang, H. Guo, C. Tian, C.-J. Sun, X.-W. Du, D. Nordlund, H. L. Xin and F. Lin, Deciphering the Cathode–Electrolyte Interfacial Chemistry in Sodium Layered Cathode Materials, *Adv. Energy Mater.*, 2018, **8**(34), 1801975.
40 L. Mu, D. Hou, E. E. Foley, M. Dai, J. Zhang, Z. Jiang, M. M. Rahman, Y. Fu, L. Ma, E. Hu, S. Sainio, D. Nordlund, J. Liu, J.-M. Hu, Y. Liu, R. J. Clément and F. Lin, Revealing the Chemical and Structural Complexity of Electrochemical Ion Exchange in Layered Oxide Materials, *J. Am. Chem. Soc.*, 2024, **146**(39), 26916–26925.
41 K. Leslie, J. Harlow, D. Rathore, K. Tuul and M. Metzger, Correlating Mn Dissolution and Capacity Fade in $LiMn_{0.8}Fe_{0.2}PO_4$/Graphite Cells During Cycling and Storage at Elevated Temperature, *J. Electrochem. Soc.*, 2024, **171**(4), 040520.
42 S. Solchenbach, G. Hong, A. T. S. Freiberg, R. Jung and H. A. Gasteiger, Electrolyte and SEI Decomposition Reactions of Transition Metal Ions Investigated by On-Line Electrochemical Mass Spectrometry, *J. Electrochem. Soc.*, 2018, **165**(14), A3304.
43 E. S. Zsoldos, D. T. Thompson, W. Black, S. M. Azam and J. R. Dahn, The Operation Window of Lithium Iron Phosphate/Graphite Cells Affects their Lifetime, *J. Electrochem. Soc.*, 2024, **171**(8), 080527.

44 W. Black, S. Azam, H. MacLennan, M. Metzger and J. R. Dahn, Understanding Capacity Loss in LFP/Graphite Pouch Cells at High Temperatures through Modelling, *J. Electrochem. Soc.*, 2025, **172**(9), 090503.
45 T. Sasaki, T. Abe, Y. Iriyama, M. Inaba and Z. Ogumi, Formation mechanism of alkyl dicarbonates in Li-ion cells, *J. Power Sources*, 2005, **150**, 208–215.
46 D. Aurbach, B. Markovsky, A. Shechter, Y. Ein-Eli and H. Cohen, A Comparative Study of Synthetic Graphite and Li Electrodes in Electrolyte Solutions Based on Ethylene Carbonate–Dimethyl Carbonate Mixtures, *J. Electrochem. Soc.*, 1996, **143**(12), 3809.
47 G. Gachot, S. Grugeon, M. Armand, S. Pilard, P. Guenot, J.-M. Tarascon and S. Laruelle, Deciphering the multi-step degradation mechanisms of carbonate-based electrolyte in Li batteries, *J. Power Sources*, 2008, **178**(1), 409–421.
48 E. S. Takeuchi, H. Gan, M. Palazzo, R. A. Leising and S. M. Davis, Anode Passivation and Electrolyte Solvent Disproportionation: Mechanism of Ester Exchange Reaction in Lithium–Ion Batteries, *J. Electrochem. Soc.*, 1997, **144**(6), 1944.
49 H. Yoshida, T. Fukunaga, T. Hazama, M. Terasaki, M. Mizutani and M. Yamachi, Degradation mechanism of alkyl carbonate solvents used in lithium-ion cells during initial charging, *J. Power Sources*, 1997, **68**(2), 311–315.
50 S. Li, X. Meng, Q. Yi, J. A. Alonso, M. T. Fernández-Díaz, C. Sun and Z. L. Wang, Structural and electrochemical properties of $LiMn_{0.6}Fe_{0.4}PO_4$ as a cathode material for flexible lithium-ion batteries and self-charging power pack, *Nano Energy*, 2018, **52**, 510–516.
51 S. Liu, J. Zheng, B. Zhang, Y. Wu, J. Liu, L. Yin, M. Zhan, Y. Xiao, B. An, L. Wang, C. Sun and X. He, Engineering manganese-rich phospho-olivine cathode materials with exposed crystal {010} facets for practical Li-ion batteries, *Chem. Eng. J.*, 2023, **454**, 139986.